3D modeling of boron transport in DIII-D L-mode wall conditioning experiments

Florian Effenberg, A. Bortolon, H. Frerichs, B. Grierson, J.D. Lore, T. Abrams, T.E. Evans, Y. Feng, R. Lunsford, R. Maingi, et al.

Nuclear Materials and Energy 26 (2021) 100900

Contents lists available at ScienceDirect

Nuclear Materials and Energy

journal homepage: www.elsevier.com/locate/nme

3D modeling of boron transport in DIII-D L-mode wall conditioning experiments

F. Effenberg [a,*], A. Bortolon [a], H. Frerichs [b], B. Grierson [a], J.D. Lore [c], T. Abrams [d], T.E. Evans [d], Y. Feng [f], R. Lunsford [a], R. Maingi [a], A. Nagy [a], R. Nazikian [a], D. Orlov [e], J. Ren [g], D.L. Rudakov [e], W.R. Wampler [h], H.Q. Wang [d]

[a] Princeton Plasma Physics Laboratory, Princeton, NJ 08543, USA
[b] University of Wisconsin - Madison, Madison, WI 53706, USA
[c] Oak Ridge National Laboratory, Oak Ridge, TN 37831, USA
[d] General Atomics, San Diego, CA 92186, USA
[e] University of California - San Diego, La Jolla, CA 92093, USA
[f] Max-Planck-Institut für Plasmaphysik, Association EURATOM IPP, 17491 Greifswald, Germany
[g] University of Tennessee, Knoxville, Knoxville, TN 37996, USA
[h] Sandia National Laboratories, Albuquerque, NM 87111, USA

ARTICLE INFO

Keywords:
Wall conditioning
Boronization
Impurity seeding
Impurity flows
EMC3-EIRENE

ABSTRACT

DIII-D L-mode experiments with local boron powder injection for real-time wall conditioning have been interpreted for the first time with the 3D plasma edge transport Monte Carlo code EMC3-EIRENE. Local B sourcing in plasma scenarios with upstream densities $1.5 \cdot 10^{19}$ m^{-3} and 2.2 MW heating results in a non-axisymmetric B distribution in the scrape-off layer (SOL) and on the divertor. The SOL frictional flows at high plasma density cause a strong inboard drag of injected impurities ($\approx$ 90%), while lower background plasma densities tend to result in a more uniform distribution. The thermal forces prevent B deposition in the near SOL while the frictional force causes B fluxes to cover the divertor plasma-facing components in a region 7–10 cm beyond the strike line. Radiative dissipation occurs for B influxes above $1 \cdot 10^{20}$ s^{-1} and causes a moderate, non-axisymmetric reduction of the far SOL divertor heat fluxes. A comparison of top and midplane B injection shows no substantial difference in inboard vs. outboard asymmetries of the B distribution. On the other hand, erosion or recycling at the strike line may distribute the boron more uniformly in the SOL.

1. Introduction

Understanding the transport and deposition of impurities released locally in the scrape-off-layer is essential for a number of applications or relevance for next-step fusion devices, including ELM-mitigation and power dissipation [1–10]. This is particularly true for real-time wall conditioning (RTWC), a technique subject of recent experimental investigation in several tokamak devices [9,11]. Conventional wall conditioning (boronization) requires evaporation of toxic borane gases (e.g., B_2D_6, $B_{10}D_{14}$) and interruption of operation, a major disadvantage concerning long-pulse steady-state reactor operation. Additionally, while this conventional technique efficiently conditions the main chamber walls, it is often less effective on divertor plasma-facing components (PFCs).

Recent advances in the study of RTWC were enabled by a versatile impurity powder dropper (IPD), designed and implemented in various machines [12], which permits to release of single or multi-species impurity powders into the SOL of fusion plasmas. The IPD can be used to inject impurities in a wide range of Z, in a non-gaseous state, including lithium, boron, boron nitride, and silicon. This work focuses on the injection of boron, the preferred material for real-time wall conditioning at DIII-D. Specifically, this study addresses the question of where the B atoms sourced in at the powder injection location are transported and deposited and how uniformly the localized impurity source can cover the main PFCs. These questions are of primary interest to evaluate the effectiveness of the technique to next-step devices such as ITER or W7-X. Due to the localization of the impurity source, the study of SOL impurity transport and wall deposition requires the use of three-dimensional models, such as those developed for stellarator research.

For this purpose, the coupled 3D plasma fluid and kinetic neutral edge transport Monte Carlo code EMC3-EIRENE is the appropriate

* Corresponding author.
E-mail address: feffenbe@pppl.gov (F. Effenberg).

https://doi.org/10.1016/j.nme.2021.100900
Received 29 October 2020; Accepted 3 January 2021
Available online 6 January 2021

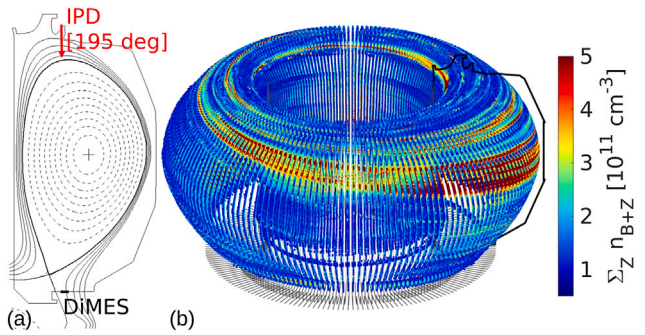

Fig. 1. (a) The lower single Null magnetic equilibrium used during real-time wall conditioning experiments. Boron has been injected with the Impurity Powder Dropper (IPD) through the small angle slot (SAS) divertor (red arrow). The DiMES probe (also pictured) was used to characterize deposited B layers in the lower divertor. (b) Example 3D distribution of total Boron density $n_B = \Sigma_Z n_{B+Z}$ in the SOL calculated with EMC3-EIRENE.

tool to address these fundamental questions [13,14]. The code can model the full torus transport of impurities and their response to the plasma background through radiative losses. EMC3-EIRENE has been widely used to analyze 3D effects in stellarator and tokamak configurations [15–23].

In order to understand the mechanisms that lead to B wall coatings by B powder injection, it is necessary to link the deposition to transport. In this work, a number of EMC3-EIRENE simulations are used to accomplish the first step towards a self-consistent model that combines the two elements.

The baseline scenario for this study is taken from a sequence of recent impurity powder injection experiments conducted at DIII-D. During the experiments, B was released gravitationally at constant rates 1–10 mg/s for 1–3 s, at a toroidal angle of $\phi_{IPD} = 195°$ [12], through a vertical aperture intersecting the closed small angle slot (SAS) divertor as indicated with the red arrow in Fig. 1. The gravitational force accelerates impurity powders downwards to 5–10 m/s before entering the SOL and undergoing ablation and ionization. Post-mortem analysis of removable witness samples in the DIII-D lower divertor, obtained with the use of the DiMES probes [24] revealed B-rich deposition films with a clear striation pattern, potentially associated with localization of the source and/or uncompensated error fields [25]. For this scenario, EMC3-EIRENE modeling is used to determine (i) the dominant B transport mechanisms in the SOL; (ii) the effect of the background plasma parameters (density) on the distribution of B fluxes and (iv) the role of radiative dissipation through B line emission. Furthermore, the questions of whether midplane injection and B layer erosion on divertor targets may affect the B flux distribution are also addressed.

In Section 2, the numerical scenario will be introduced. The 3D distribution of Boron in the SOL and on the divertor is analyzed in Sections 3, and 4, respectively. The main transport mechanisms and the effects on the plasma background are analyzed in Sections 5, and 4. The effects of sourcing from upstream midplane and downstream are considered in Section 7, and a final summary of the conclusions is provided in Section 8.

2. Implementation of the reference scenario in EMC3-EIRENE

The scenario (179894 at 3.500 s) considered for numerical modeling is a lower single null reversed B_t L-mode plasma on the DIII-D tokamak ($R = 1.7$ m, $a = 0.6$ m) with neutral beam power $P_{NB} = 2.2$ MW, $B_{tor} = 2$ T, $q_{95} = 4.6$ and a volume-averaged density of $\bar{n} \approx 3 \cdot 10^{19}$ m^{-3}. A 2D equilibrium has been reconstructed with the kinetic equilibrium reconstruction module kineticEFITtime in the OMFIT analysis framework [26]. Representative magnetic flux surfaces are shown in Fig. 1(a). The impurity injection has been modeled in most cases as

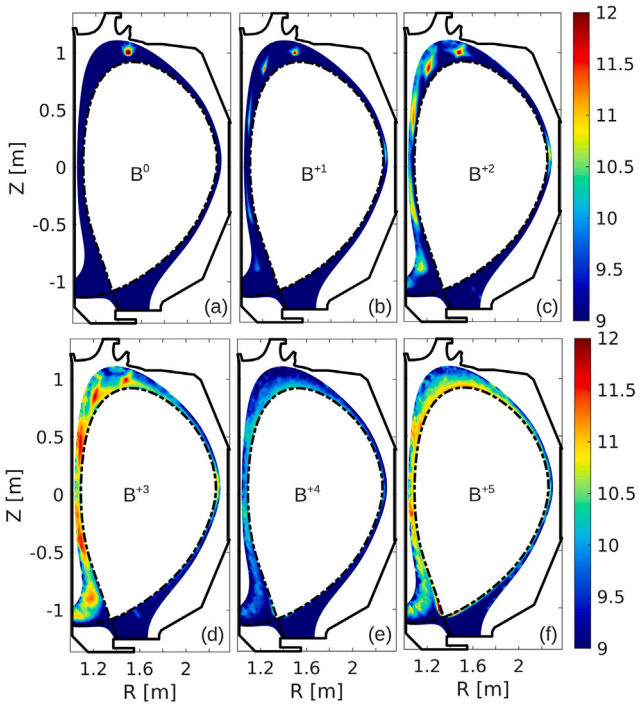

Fig. 2. Densities of (a) neutral Boron B^0 and (b-f) ionized Boron $B^{+1} - B^{+5}$ at the toroidal injection location (195°).

a point source at $R = 148.4$ cm and $Z = 100.2$ cm, but, as described below, impurity injection from the midplane ($R = 227.2$ cm, $Z = 0$ cm) was also considered. Lastly, B erosion from the divertor targets has been considered.

The equilibrium has been extended to a full-torus (360°) computational grid for dedicated 3D transport studies with the fully 3D coupled plasma fluid and kinetic edge transport Monte Carlo code EMC3-EIRENE. A reduced, 40°-toroidal segment was used to investigate features that do not require the full toroidal resolution (e.g., inboard vs. outboard relative flux distributions for low B radiation or B erosion). EMC3 solves a set of reduced Braginskii fluid equations for particles, parallel momentum, and energies for electrons and ions [27]. EIRENE solves the kinetic transport equations for neutral atoms and molecules, including collisional processes [14]. It has to be noted that the present 3D model does not include ∇B and E×B drift effects. These drift effects may affect the flow structure and divertor fluxes according to 2D modeling [28,29]. The impurity injection and impurity transport have been treated by the impurity trace fluid model in this study. The impurity source strength has been defined as a fixed influx rate Γ_B corresponding to experimental values ($1 \cdot 10^{19} - 1 \cdot 10^{20}$ s^{-1}) or an effective sputtering yield Y_B. Once the neutral impurities are released and ionized, their transport is modeled by the trace impurity fluid module. Here, a fluid momentum balance equation is solved, and the impurities impact the main plasma species by ionization and excitation through a loss term in the energy balance equation. The following continuity and momentum equations are solved:

$$\nabla_{\parallel} \cdot (n_z V_{z\parallel}) + \nabla_{\perp} \cdot (-D_{imp} \nabla_{\perp} n_z) = S_z \tag{1}$$

$$\begin{aligned} 0 = & -\frac{1}{n_z}\frac{dp_z}{ds} + ZeE_{\parallel} + m_z \frac{V_{\parallel} - V_{z\parallel}}{\tau_{zi}} \\ & +0.71Z^2\frac{dT_e}{ds} + 2.6Z^2\frac{dT_i}{ds} \\ & = F_P + F_E + F_{fr} + F_{th,e} + F_{th,i} \end{aligned} \tag{2}$$

where S_z represents the impurity ionization source for charge state Z, and D_{imp} is the anomalous particle diffusivity. $\tau_{zi} = \frac{1.47 \cdot 10^{13} m_z (T_i^3/m_i)^{0.5}}{(1+m_i/m_z) n_i Z^2 ln\Lambda}$

($ln\Lambda \approx 15$) is the collision time between impurities and background main ions [30].

The terms in Eq. (2) correspond to pressure force F_P, electric force F_E, friction force F_{fr} and electron and ion thermal force $F_{th,e}$ and $F_{th,i}$, respectively. The impurity ion temperatures are assumed to be equal to the background main ion temperature ($T_z = T_i$).

The impurity force balance in Eq. (2) can in a steady-state be directly expressed by the resulting parallel impurity flow velocity:

$$V_{z\parallel} = V_\parallel + \frac{\tau_{zi} Z^2}{m_z}\left(0.71\frac{dT_e}{ds} + 2.6\frac{dT_i}{ds}\right) + \frac{\tau_{zi} Ze}{m_z} E_\parallel - \frac{\tau_{zi}}{n_z m_z}\frac{dT_i}{ds} n_z \quad (3)$$

The electrostatic force and pressure force can be neglected in most plasma edge scenarios [15]. This simplifies Eq. (3) with $\tau_{zi} \propto Z^{-2}$ to a force balance that is determined by the friction and ion thermal forces only and that is not dependent on the charge state Z anymore:

$$V_{z\parallel} \approx V_\parallel - \alpha\frac{dT_i}{ds} = V_{fr} - V_{i-th} \quad (4)$$

with the flows V_{fr} and V_{i-th} induced by F_{fr} and F_{i-th}, respectively.

A 1D core transport model [27] is used to model further ionization of impurities inside the core plasma based on a prescribed density and temperature profiles obtained from the experiment.

While the field geometry is axis-symmetric in this model, the impurity ion traces break the 2D symmetry. A typical example of the 3D non-axisymmetric total B density $n_B = \Sigma_Z n_{B+Z}$ is shown in Fig. 1(b). The highest B concentration follows a spiral-like trace from the source down to the divertor. The transport of boron will be discussed in more detail in the following section.

3. Non-axisymmetric boron flux distribution

As a starting point, the plasma and neutral transport have been calculated for the reference scenario without impurity injection. An upstream density of $n_{up} \approx 1.5 \cdot 10^{19}$ m^{-3} was set based on measurements with Thomson Scattering. The anomalous particle and heat cross-field transport in the plasma edge was prescribed by $D_\perp = 0.33$ m^{2}s^{-1} and $\chi_\perp = 1.0$ m^{2}s^{-1}. Boron impurities are released with an influx rate of $\Gamma_B = 10^{19} - 10^{20}$ s^{-1}. The B cross-field particle diffusivity is the same as the one of the main ion species ($D_{B,\perp} = 0.33$ m^{2}s^{-1}), and no recycling is assumed. The source distribution (neutral B density) is shown in Fig. 2(a). The complete set of ionization stages is shown in Fig. 2(b–f) for B^{+1}- B^{+5}. The distribution shows higher concentrations in the SOL for the three lower charge states, which have ionization energies in the range 8–38 eV. For smaller B injections, which may not change the SOL temperatures significantly, the plasma distribution shows the highest Boron concentration at the high field side. The source locations and parameters have been varied to investigate the effect on the distribution and the deposition. Vertical displacements of the B source (corresponding to deeper penetration of B particles) and changes of the source energy (covering a range of $0.1 - 100$ eV) or distribution function (point source vs. beam source) do not result in substantial changes of this B flux distribution. Dissipation through radiative losses may also affect the transport properties, but typically with second-order effects. Overall, the simulations show that typically 90% of the total B flux reaching the inboard target.

4. 3D deposition of boron on the divertor PFCs

In general, parallel plasma flows drive the impurities down to the targets, whereas anomalous cross-field transport broadens the impurity distribution in the plasma edge and eventually on the targets. A mapping of the total boron impurity fluxes $\Gamma_B \approx \Sigma_Z n_{B+Z} V_{B+Z,\parallel}$ onto the inner and outer target is shown in Fig. 3(a, b) in a $\phi_{tor} - Z$-, and a $\phi_{tor} - R$-mapping, respectively. The 3D modeling results show that most (> 90%) of the B flux goes to the inner target (Fig. 3(a)).

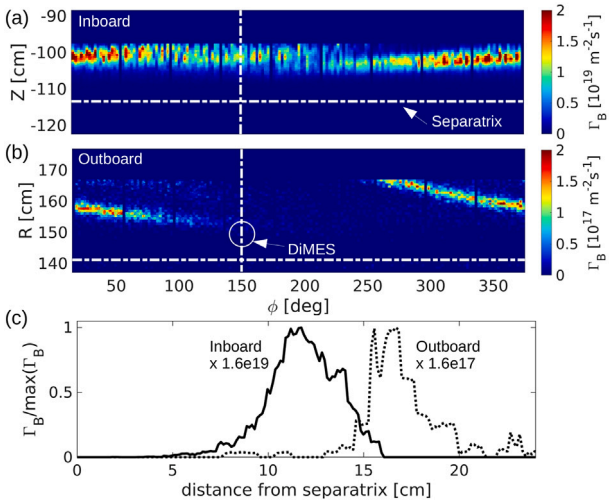

Fig. 3. (a) Mapping of Boron impurity fluxes Γ_B on the inner/vertical target. (b) Mapping of Boron impurity fluxes Γ_B on the outer/horizontal divertor. The horizontal dashed lines indicate the separatrix position. (c) Sample profiles of the fluxes taken at 145° (DiMES position) on the inner and outer divertor.

This primarily inboard-directed SOL impurity flux has also been found during former experiments with toroidally symmetric methane ($^{13}CH_4$) gas injection [31–33]. The B deposition zone starts about 7 cm beyond the strike line and covers approximately 10 cm in the far SOL (the strike line at $R = 142$ cm is shown as a dashed line). The radially and toroidally non-uniform patterns are found, with the radial location of the peak B flux varying diagonally across the targets. These non-axisymmetric deposition patterns in an otherwise symmetric plasma result from the localization of the source mediated by the competing mechanisms of cross-field ionization and diffusive transport, and fast parallel transport.

The position of the DiMES probe is marked by a circle (Fig. 3(b)). In this scenario, it happens that the DiMES probe would be exposed only to the radially innermost tail of the initial B flux. A 1D perpendicular B flux profile at the toroidal DiMES location (marked by the circle in the 2D mapping) is shown in Fig. 3(c) for inner (solid line) and outer (dashed line) divertor. The DiMES radial location is $R_{DiMES} = 147 - 152$ cm, and approximately half of the primary peak overlaps with the DiMES surface. The large scale striation in the modeling does not explain the experimentally observed small scale striations on the DiMES probe, which might be associated with intrinsic error fields. The ratio between inner and outer divertor total B fluxes varies by 1–2 orders of magnitude and also shows a strong variation in toroidal direction on the outer target. The near SOL region (first few centimeters beyond strike line) remains weakly exposed to the B flux.

In this study, it is assumed that the B surface deposition rate during an injection is represented by the local divertor fluxes to the targets. In particular, the effects of recycling, erosion, and further migration are neglected. While this allows a straightforward interpretation of the results, the accuracy of the prediction is limited to locations that are several plasma decay lengths into the SOL, where recycling and erosion play a marginal role.

The aforementioned dependence of the boron flux distribution on the radial B source location has been investigated by shifting the source location in the vertical direction between $Z = 95.2 - 107.2$ cm. The main features of the B flux distribution remain qualitatively the same. A radial inward shift of the impurity source appears to decrease the flux to the targets. The causes of this insensitivity are the SOL impurity forces discussed in the following.

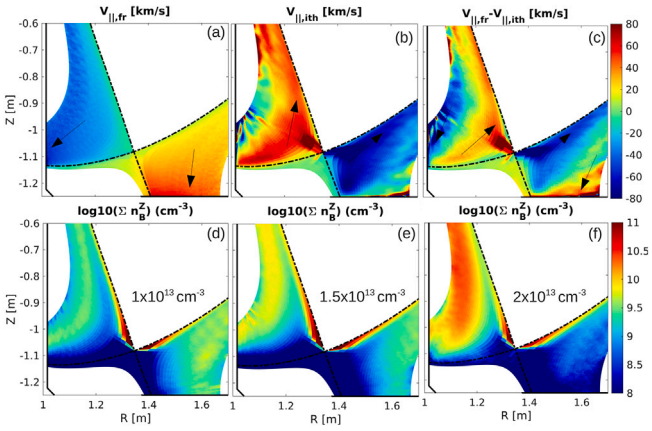

Fig. 4. (a) Parallel impurity velocity associated with the ion thermal gradient force $V_{\parallel,ith}$. (b) Parallel impurity velocity associated with the friction force $V_{\parallel,fr}$. (c) Difference between $V_{\parallel,ith}$ and $V_{\parallel,fr}$. (d) Boron density for low (e) medium and high (f) upstream density.

5. Role of frictional flow on B deposition location

The impurity transport was analyzed for different plasma densities to understand the effect of the dominant forces on the B flux distributions. The leading components of Eq. (4) and their difference are shown in Fig. 4(a–c) for the default density scenario. The frictional flow velocity $V_{\parallel,fr}$ shown in Fig. 4(a) is mostly directed to the targets and counter-directed in the parallel direction (positive vs. negative sign). The distribution of the ion-thermal force flow component $V_{\parallel,ith}$ is shown in Fig. 4(b). It has opposite signs with respect to the frictional flow and is strong close to the separatrix. The difference of these two flow components $V_{\parallel,fr} - V_{\parallel,ith}$ is shown in Fig. 4(c) and reveals the dominance of $V_{\parallel,ith}$ in the near SOL and of $V_{\parallel,fr}$ in the far SOL. This analysis of the leading parallel impurity force terms shows that the ion thermal force $F_{th,i}$ dominates in the hot SOL close to the separatrix. In contrast, the frictional force F_{fr} is strong in the far and remote SOL (see Eq. (3)). Impurities in the near SOL region are driven to the upstream by the ion thermal force. When they accumulate upstream, they may enter the confinement region and dilute the core plasma. At the same time, they also diffuse outwards into the far SOL. Impurities sourced or diffusing into the far SOL are subject to the frictional flows and dragged to the divertor. The frictional flows thereby provide a major screening mechanism preventing core impurity accumulation and cause the deposition on the divertor wetted by the far SOL. The ion thermal force, however, prevents deposition in the vicinity of the strike lines. The balance of these competing forces is what determines the radial B flux distribution in Fig. 3.

These two force components governing the B fluxes cannot be controlled directly. However, changes in the background density affect the collisionality and transport and thereby the relative strengths and distributions of the impurity forces. Fig. 4 (d–e) shows the total B density distributions resulting from varying the plasma background density in the range of $1.0-2.0\cdot10^{19}$ m^{-3}. A Lower main species density reduces the frictional flows and initial ionization resulting in a more even distribution of B fluxes onto the high field and low field side PFCs (Fig. 4(d)). Conversely, higher densities enhance the friction force and initial ionization, which causes a stronger accumulation on the inboard side Fig. 4(f)). These results suggest that lower collisionality favors a more uniform B distribution in the SOL and between the inboard and outboard divertor targets.

6. 3D radiative cooling effects on divertor fluxes

In general, any B concentration is accompanied by an amount of radiative losses $P_{rad,B} \propto \Sigma_Z L_Z n_e n_{B+Z}$, typically associated with line emission. Here, potential cooling effects caused by B isotropic line emission are investigated. Indeed, the modeling shows substantial changes in the far SOL plasma distribution due to radiative dissipation in the flux tubes fueled with boron. B injection rates above $\Gamma_B \approx 10^{19}$ s^{-1} result in a perturbation on the plasma background due to increasing isotropic line emission. SOL temperature losses of about 10 eV affect the parallel thermal pressure $n(T_e + T_i)$, and reduce the heat fluxes q_{div} to the inner and outer divertor targets.

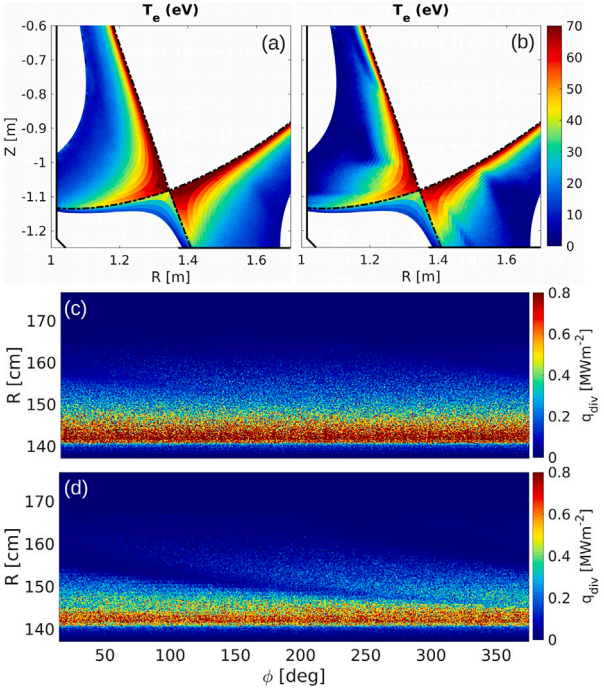

Fig. 5. (a) Cooling effects on electron temperature distribution for medium B influx. (b) Cooling effects on electron temperature distribution for high B influx. (c) Cooling effects on outer divertor heat flux for medium B influx. (d) Cooling effects on outer divertor heat flux for high B influx.

The distribution of the electron temperature in the divertor region is shown for cases with medium and relatively high influx rate of $\Gamma_B = 10^{20}$ and 10^{21} s^{-1} in Fig. 5(a) and (b), respectively. The radiative cooling affects mostly the temperature distribution in the far SOL, as it is clearly evident for T_e in Fig. 5(b). The divertor heat flux distributions depicted in Fig. 5(c) and (d) show a reduction in the outer tails of the outer divertor heat fluxes but not at the strike line position. The distribution of radiative losses follows the distribution of B fluxes. Similar non-axisymmetric cooling effects on the divertor fluxes were also found in a 3D modeling study of Alcator C-Mod H-mode plasmas with strong nitrogen seeding [34]. A detailed assessment of these cooling effects is beyond the main scope and purpose. Nevertheless, these effects show that high B influx rates can have a non-axisymmetric perturbative response on the plasma background. Therefore, B might be considered as a means to induce momentum losses in future experiments.

7. Other sources: midplane injection and erosion

The effects of substantial changes in the B source location on the B distribution have been investigated. Midplane injection has been considered as an alternative to the top injection for future experiments. For this purpose, an atomic B point source has been defined at $R = 227.2$ cm and $Z = 0.0$ cm. The qualitative features of the resulting B density distribution shown in Fig. 6(a) are very similar to the ones obtained with the top injection. Despite B being released on the outboard side, most flux is dragged to the inboard side. This result suggests that the

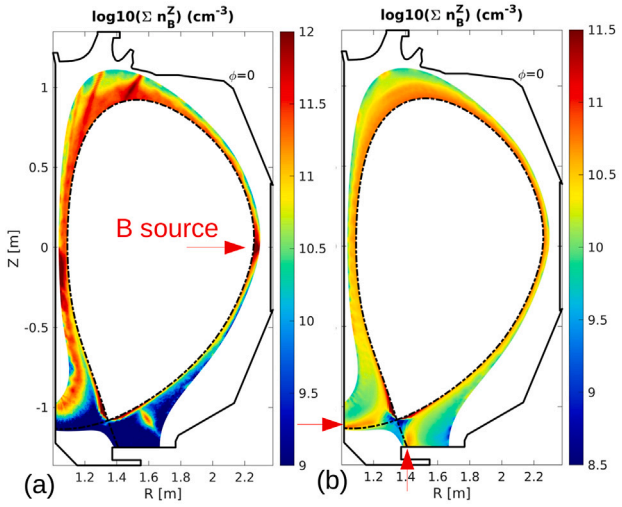

Fig. 6. Total boron density for (a) B midplane injection, and (b) B erosion from targets. The red arrows mark the source locations.

upstream flow structure generally causes inboard accumulation of the B.

A substantial change in the B distribution is found if B is sourced at the strike lines through erosion (corresponding to a uniform B coating prior to plasma exposure). A sputtering yield of $Y_B = 2\%$ is assumed resulting in a total B influx of $\Gamma_B \approx 6 \cdot 10^{19} s^{-1}$. The distribution depicted in Fig. 6(b) shows a much more uniform distribution and strong upstream accumulation of B. The maximum B erosion occurs at the strike line locations causing a B density distribution, which decays strongly in the far SOL. The ion-thermal force enhances the upstream drag and accumulation in the near SOL. At the same time, diffusive cross-field transport drives B outwards into the far SOL, which is dominated by frictional flows. This suggests that B re-erosion has the effect of re-distributing B impurities more uniformly between the inner and outer targets, which is beneficial for RTWC applications.

8. Summary and conclusions

A first assessment of local impurity injection for wall-conditioning L-mode experiments has been conducted with EMC3-EIRENE simulations. The local injection of atomic boron results in a non-axisymmetric B distribution in the SOL and the divertor.

The far SOL transport largely determines the initial distribution of locally seeded impurities. The ion thermal force drives boron upstream and prevents initial deposition close to the strike line. The frictional flows in the far SOL drag the impurities to the divertor and determine the deposition profile.

The results show that the distribution of B can be controlled by appropriately tailoring the density of the plasma. The boron density and divertor fluxes show a more even distribution in case of lower collisionality. In contrast, higher densities cause a more localized concentration of B and enhanced drag to the inboard side ($\geq 90\%$ of Γ_B in the scenarios considered).

The radial cross-field distribution is only marginally sensitive to a vertical displacement of the source location. The primary deposition occurs in the region $R - R_{sep} = 7$–10 cm several plasma decay lengths beyond the main erosion zone (strike line location) on the inner and outer divertor target. The deposition pattern does, however, not explain (potentially error field related) small scale striation patterns found on DiMES in the experiment.

Isotropic boron radiation occurs in the far SOL and can substantially modify the 3D electron temperature distribution. The divertor heat and particle flux tails also show a non-axisymmetric decrease in response to the enhanced dissipation.

Variation of the source location in the upstream region does not substantially affect the B distribution for the default density scenario. In contrast, B sourcing at the strike line results in a relatively uniform distribution of the B, suggesting that erosion and recycling are crucial for even coverage of the main plasma wetted areas.

Under the assumptions of a local impurity source, no recycling, and no erosion, the modeling suggests that the B fluxes might not reach the near SOL and even leave toroidal gaps in the far SOL coatings. However, the assumption of a single source will have to be extended to multiple source locations due to macroscopic particle (dust-like) transport. Here, coupling of EMC3-EIRENE with the DUSTT code [35] is a promising next step to add the complexity of particle migration, eventually introducing the distribution of various local impurity sources in powder-dropping experiments. Furthermore, the effects of recycling and re-erosion should be considered to be conclusive about the final deposition resulting from real-time wall conditioning in current fusion device experiments.

Declaration of competing interest

The authors declare that they have no known competing financial interests or personal relationships that could have appeared to influence the work reported in this paper.

Acknowledgments

This work was supported by the United States Department of Energy (DoE) under Grants No. DE-AC02-09CH11466, DE-AC05-00OR22725, DE-SC0020357, DE-SC0020284, DE-FC02-04ER54698, DE-FG02-07ER 54917, DE-NA0003525, and DE-SC0019256.

Disclaimer

References

[1] A. Kallenbach, R. Dux, V. Mertens, O. Gruber, G. Haas, M. Kaufmann, W. Poschenrieder, F. Ryter, H. Zohm, M. Alexander, K. Behringer, M. Bessenrodt-Weberpals, H.-S. Bosch, K. Buchl, A. Field, J. Fuchs, O. Gehre, A. Herrmann, S. Hirsch, W. Koppendorfer, K. Lackner, K. Mast, G. Neu, J. Neuhauser, S.D.P. Hempel, G. Raupp, K. Schonmann, A. Stabler, K.-H. Steuer, O. Vollmer, M. Weinlich, W. West, T. Zehetbauer, Nucl. Fusion 35 (10) (1995) 1231–1246.

[2] J. Rapp, T. Eich, M. von Hellermann, A. Herrmann, L.C. Ingesson, S. Jachmich, G.F. Matthews, V. Philipps, G. Saibene, contributors to the EFDA-JET Workprogramme, Plasma Phys. Control. Fusion 44 (6) (2002) 639–652.

[3] M. Reinke, J. Hughes, A. Loarte, D. Brunner, I. Hutchinson, B. LaBombard, J. Payne, J. Terry, J. Nuclear Mater. 415 (1, Supplement) (2011) S340 – S344, Proceedings of the 19th International Conference on Plasma-Surface Interactions in Controlled Fusion.

[4] A. Kallenbach, M. Bernert, R. Dux, L. Casali, T. Eich, L. Giannone, A. Herrmann, R. McDermott, A. Mlynek, H.W. Müller, F. Reimold, J. Schweinzer, M. Sertoli, G. Tardini, W. Treutterer, E. Viezzer, R. Wenninger, M. Wischmeier, Plasma Phys. Control. Fusion 55 (12) (2013) 124041.

[5] T. Petrie, S. Allen, M. Fenstermacher, R. Groebner, C. Holcomb, E. Kolemen, R.L. Haye, C. Lasnier, A. Leonard, T. Luce, A. McLean, R. Maingi, R. Moyer, W. Solomon, V. Soukhanovskii, F. Turco, J. Watkins, J. Nuclear Mater. 463 (2015) 1225–1228, Plasma-Surface Interactions 21.
[6] H. Wang, H. Guo, T. Petrie, A. Leonard, D. Thomas, J. Watkins, Nuclear Mater. Energy 12 (2017) 942–947, Proceedings of the 22nd International Conference on Plasma Surface Interactions 2016, 22nd PSI.
[7] R. Maingi, J. Hu, Z. Sun, K. Tritz, G. Zuo, W. Xu, M. Huang, X. Meng, J. Canik, A. Diallo, R. Lunsford, D. Mansfield, T. Osborne, X. Gong, Y. Wang, Y. Li, Nucl. Fusion 58 (2) (2018) 024003.
[8] F. Effenberg, S. Brezinsek, Y. Feng, R. König, M. Krychowiak, M. Jakubowski, H. Niemann, V. Perseo, O. Schmitz, D. Zhang, T. Barbui, C. Biedermann, R. Burhenn, B. Buttenschön, G. Kocsis, A. Pavone, F. Reimold, T. Szepesi, H. Frerichs, Y. Gao, U. Hergenhahn, S. Kwak, M. Otte, T.S. Pedersen, Nucl. Fusion 59 (10) (2019) 106020.
[9] A. Bortolon, V. Rohde, R. Maingi, E. Wolfrum, R. Dux, A. Herrmann, R. Lunsford, R. McDermott, A. Nagy, A. Kallenbach, D. Mansfield, R. Nazikian, R. Neu, Nuclear Mater. Energy 19 (2019) 384–389.
[10] R. Lunsford, et al., 2020 Bulletin of the American Physical Society 62 (2020).
[11] A. Bortolon, R. Maingi, A. Nagy, J. Ren, J. Duran, A. Maan, D. Donovan, J. Boedo, D. Rudakov, A. Hyatt, T. Wilks, M. Shafer, C. Samuell, M. Fenstermacher, E. Gilson, R. Lunsford, D. Mansfield, T. Abrams, R. Nazikian, Nuclear Fusion 60 (12) (2020) 126010.
[12] A. Nagy, A. Bortolon, D.M. Mauzey, E. Wolfe, E.P. Gilson, R. Lunsford, R. Maingi, D.K. Mansfield, R. Nazikian, A.L. Roquemore, Rev. Sci. Instrum. 89 (10) (2018) 10K121.
[13] Y. Feng, F. Sardei, J. Kisslinger, J. Nuclear Mater. 266–269 (1999) 812–818.
[14] D. Reiter, Technical Report Jül-1947, Forschungszentrum Jülich, 1984.
[15] Y. Feng, F. Sardei, P. Grigull, K. McCormick, J. Kisslinger, D. Reiter, Nucl. Fusion 46 (8) (2006) 807.
[16] H. Frerichs, D. Reiter, O. Schmitz, T. Evans, Y. Feng, Nuclear Fusion 50 (3) (2010) 034004.
[17] J. Lore, J. Canik, Y. Feng, J.-W. Ahn, R. Maingi, V. Soukhanovskii, Nucl. Fusion 52 (5) (2012) 054012.
[18] T. Lunt, Y. Feng, M. Bernert, A. Herrmann, P. de Marné, R. McDermott, H. Müller, S. Potzel, T. Pütterich, S. Rathgeber, W. Suttrop, E. Viezzer, E. Wolfrum, M. Willensdorfer, the ASDEX Upgrade team, Nucl. Fusion 52 (5) (2012) 054013.
[19] M. Kobayashi, S. Masuzaki, I. Yamada, Y. Narushima, C. Suzuki, N. Tamura, B. Peterson, S. Morita, C. Dong, N. Ohno, S. Yoshimura, Y. Feng, M. Goto, K. Sato, T. Akiyama, K. Tanaka, the LHD experiment group, Nucl. Fusion 53 (9) (2013) 093032.
[20] H. Frerichs, O. Schmitz, I. Waters, G.P. Canal, T.E. Evans, Y. Feng, V.A. Soukhanovskii, Phys. Plasmas 23 (6) (2016) 062517.
[21] M. Shoji, G. Kawamura, H. Tanaka, I. Watanabe, M. Kobayashi, M. Tokitani, S. Masuzaki, LHD Experiment Group, Contrib. Plasma Phys. 56 (6-8) (2016) 651–656.
[22] O. Schmitz, M. Becoulet, P. Cahyna, T. Evans, Y. Feng, H. Frerichs, A. Loarte, R. Pitts, D. Reiser, M. Fenstermacher, D. Harting, A. Kirschner, A. Kukushkin, T. Lunt, G. Saibene, D. Reiter, U. Samm, S. Wiesen, Nucl. Fusion 56 (6) (2016) 066008.
[23] F. Effenberg, Y. Feng, O. Schmitz, H. Frerichs, S. Bozhenkov, H. Hölbe, R. König, M. Krychowiak, T.S. Pedersen, D. Reiter, L. Stephey, W7-X Team, Nucl. Fusion 57 (3) (2017) 036021.
[24] D. Rudakov, T. Abrams, R. Ding, H. Guo, P. Stangeby, W. Wampler, J. Boedo, A. Briesemeister, J. Brooks, D. Buchenauer, I. Bykov, C. Chrobak, R. Doerner, D. Donovan, J. Elder, M. Fenstermacher, J. Guterl, E. Hinson, E. Hollmann, C. Lasnier, A. Leonard, A. McLean, R. Moyer, R. Nygren, D. Thomas, E. Unterberg, J. Watkins, C. Wong, Fusion Eng. Des. 124 (2017) 196–201, Proceedings of the 29th Symposium on Fusion Technology (SOFT-29) Prague, Czech Republic, September 5-9, 2016.
[25] A. Bortolon, et al., 2019 Bulletin of the American Physical Society 64 (2019).
[26] O. Meneghini, S. Smith, L. Lao, O. Izacard, Q. Ren, J. Park, J. Candy, Z. Wang, C. Luna, V. Izzo, B. Grierson, P. Snyder, C. Holland, J. Penna, G. Lu, P. Raum, A. McCubbin, D. Orlov, E. Belli, N. Ferraro, R. Prater, T. Osborne, A. Turnbull, G. Staebler, Nucl. Fusion 55 (8) (2015) 083008.
[27] Y. Feng, H. Frerichs, M. Kobayashi, A. Bader, F. Effenberg, D. Harting, H. Hoelbe, J. Huang, G. Kawamura, J.D. Lore, T. Lunt, D. Reiter, O. Schmitz, D. Sharma, Contrib. Plasma Phys. 54 (4–6) (2014) 426–431.
[28] A. Jaervinen, S. Allen, M. Groth, A. McLean, T. Rognlien, C. Samuell, A. Briesemeister, M. Fenstermacher, D. Hill, A. Leonard, G. Porter, Nuclear Mater. Energy 12 (2017) 1136–1140, Proceedings of the 22nd International Conference on Plasma Surface Interactions 2016, 22nd PSI.
[29] E. Kaveeva, V. Rozhansky, I. Senichenkov, E. Sytova, I. Veselova, S. Voskoboynikov, X. Bonnin, R. Pitts, A. Kukushkin, S. Wiesen, D. Coster, Nucl. Fusion 60 (4) (2020) 046019.
[30] P.C. Stangeby, The Plasma Boundary of Magnetic Fusion Devices, in: Plasma Physics Series, Nicki Dennis, Institute of Physics Publishing, Philadelphia, 2000.
[31] S. Allen, W. Wampler, A. McLean, D. Whyte, W. West, P. Stangeby, N. Brooks, D. Rudakov, V. Phillips, M. Rubel, G. Matthews, A. Nagy, R. Ellis, A. Bozek, J. Nuclear Mater. 337–339 (2005) 30–34, PSI-16.
[32] J. Elder, P. Stangeby, D. Whyte, S. Allen, A. McLean, J. Boedo, B. Bray, N. Brooks, M. Fenstermacher, M. Groth, C. Lasnier, S. Lisgo, D. Rudakov, W. Wampler, J. Watkins, W. West, J. Nuclear Mater. 337–339 (2005) 79–83, PSI-16.
[33] W. Wampler, A. McLean, S. Allen, N. Brooks, J. Elder, M. Fenstermacher, M. Groth, P. Stangeby, W. West, D. Whyte, J. Nuclear Mater. 363–365 (2007) 72–77, Plasma-Surface Interactions-17.
[34] J.D. Lore, M.L. Reinke, D. Brunner, B. LaBombard, B. Lipschultz, J. Terry, R.A. Pitts, Y. Feng, Phys. Plasmas 22 (5) (2015) 056106.
[35] A.Y. Pigarov, S.I. Krasheninnikov, T.K. Soboleva, T.D. Rognlien, Phys. Plasmas 12 (12) (2005) 122508.